Chapter 2

Accelerating protons from a mass limited spherical target using an ultrashort laser pulse

The work included in this chapter is published in A. Bhagawati, et al. "Proton acceleration due to laser plasma interactions from mass-limited spherical targets." Physics of Plasmas 26.9, 093106 (2019).

The proton acceleration processes involved in the interaction of an ultrashort circularly polarized laser with a near-critical density spherical target are investigated in this chapter using three dimensional particle in cell simulations. Both the target size and the target density are observed to be crucially governing the dynamics of the fast protons. The relativistically induced transparency helps in a stronger heating of the target and a complicated interplay is observed between the participating interaction processes. The generation of hot-electrons and their re-circulations within the plasma help in the formation of shocks which exerts a further push to the protons accelerated by the electrostatic sheath formed due to the ponderomotive force. A maximum peak proton energy of about 40 MeV is observed which is the result of the cumulative effects of the shock and sheath acceleration. Electron jets are observed in the forward laser direction for a larger target size, which suppresses the energy of the proton beams.

2.1 Accelerating ions from mass-limited targets

Targets having compressed transverse dimensions (comparable to the laser spot size), also known as mass-limited targets (MLT), have been largely used in the study of generation of energetic ion beams. Their use has greatly displayed an increase in the efficiency of the ion beam energy with a significant rise in the peak energy, as compared to extended foil targets with equal thicknesses [1, 2]. The use of MLT has reduced the lateral expansion of hot electrons by reducing the surface of the target. The electrons are thus confined to a lesser space for a longer time which ultimately increases the accelerating field. This noticeably reduces the unwanted widening of the sheath beyond the laser focus area. Various studies have been done using MLTs and ultrashort laser pulses, which shows significant improvement in the generation of fast particles, compared to thick targets [3, 4, 5]. The interaction mechanism is greatly influenced by the small size and geometry of the mass limited targets [6, 7]. Recently, spherical plasma targets have been explored to obtain energetic particle beams due to interactions with laser [3, 5, 8, 9, 10]. Electron heating is not powerful in the case of a large spherical target as the electrons cool down fast and exhaust the recirculation process, leading to a depletion in the ion energy [2]. It has been found from previous studies that, a spherical target for which the diameter is of the order of the laser spot size, facilitates the production of fast ions [1]. Additionally, it has been found that when the target diameter is slightly less than the laser focal spot size, the divergence of the ion beam is significantly reduced along with the enhancement of the peak ion energy [11, 12]. However, these studies are performed using solid density spheres. It has been established that a near-critically dense plasma facilitates the formation of strong shocks, that leads to the acceleration of the ions from the shock fronts. Therefore, in the present study we utilised a plasma sphere of relativistically near-critical density to investigate the generation of energetic ion bunches.

In this chapter, we used three dimensional particle in cell (PIC)

simulation to study the influence of target parameters and the laser polarization on the ion acceleration processes occurring when a pulsed femtosecond laser interacts with a mass limited near-critically dense spherical target. The topic of proton acceleration by laser-driven shocks in spherical plasma targets of near-critical density has not received sufficient attention. The presented work was motivated by the experimental observation of strongly directed proton beam emitted from spherical mass-limited target by Henig et al. [10] which revealed that ions gain energy due to shocks formed in plasma as indicated by a plateau-shaped energy spectrum. In the experiment, a highly collimated proton beam with plateau-shaped spectrum extending to energies upto 8 MeV was observed.

In the present work, a detailed study is made on the dependence of the quality of the proton beam on the diameter and density in the near-critical regime of the spherical plasma target. The study reveals that the energy gained by the proton beam crucially depends on the shape, size and density of the plasma target. Moreover, a circularly polarized laser is found to be more effective in accelerating the particles than a linearly polarized beam. Three main types of proton acceleration mechanisms are observed in this work, where the protons get accelerated from the front surface, the central portion of the target or from the rear surface. There are clear observation of the formation of shocks, which accelerated the ions to twice the shock velocity. The density in the relativistically near-critical regime supports the generation of the shock and assists the production of energetic ions. A comparative study is also made between the maximum energy obtained from a spherical target with that of a planar target having equal dimensions.

2.2 Laser-driven electrostatic shock in near-critical plasma

An electrostatic shock wave is created in plasma due to a sudden rise in density which is accompanied by the onset of a sharp electric field [13]. When an intense laser beam interacts with an over-dense [14, 15, 16] or near-critical [13, 17] plasma target, the laser gets stopped near the critically-dense layer. The radiation pressure of the laser pushes the plasma electrons into the target creating a density perturbation in the plasma. A shock wave is characterized by a sharp electric field in the pressure transition region and may reflect ions and accelerate to twice the shock velocity. Usually, ion acoustic waves (IAW) in plasma may manifest as shock waves when amplitude grows and plasma particles are trapped resulting in high amplitude electric field. The ions upstream of the shock are reflected from it if the shock reflection condition is satisfied, i.e. if the electrostatic potential energy, $Ze\Phi_{max}$ associated with the shock front is higher than the kinetic energy of the upstream ions, $\frac{1}{2}mv_i^2$. Here v_i is the velocity of the ions in the shock frame. These ions get reflected elastically to twice the shock velocity leading to ion acceleration [18].

In the case of near-critical plasma, the shock formation usually takes place at later times as compared to over dense targets [13]. For $a_0 > \frac{n_e}{n_c}$, the relativistic transparency becomes dominant over the radiation pressure action initially. After a considerable amount of time, plasma electrons get accumulated ahead of the circularly polarized laser pulse due to the ponderomotive force. The region becomes electron-rich creating a strong unipolar electric field which results in the accumulation of ambient ions just ahead of the laser front, forming an ion density peak. This might lead to the development of a shock which travels at supersonic velocity, i.e. with Mach number $1.5 < M < 3.5$ [30]. Generally, the shock travels with velocity higher than the hole-boring velocity $v_s > v_{hb}$ and so the shock accelerated ions have energies higher than the hole-boring ions [21]. The two basic conditions for collisionless electrostatic shock

formation are (a) there should be a uniform electron heating followed by recirculation of hot electrons and (b) a sharp variation in plasma density [10, 17]. The presence of such a shock may be identified from the ion phase space. High-velocity shocks can accelerate ions to very large velocities, with $M > 1.5$ [21].

In order to obtain shocks with high velocity, the electrons need to be heated uniformly. For solid density targets, the hot electrons are generated at the vacuum-target surface which is followed by collisionless heating processes to ignite the entire target. However, in the case of near-critically dense target, a significant amount of the laser energy can get absorbed in the plasma and effectively produce energetic electrons [17]. As the laser is stopped around critical density, it steepens the plasma profile and heats the electrons efficiently. The heated electrons move to the backside of the target, perturbs the background plasma and drives a return current. This fast return current plays important role in heating the entire plasma volume, which is a precursor to the onset of shock wave. Due to stronger coupling and volumetric heating, generation of hot electrons is very efficient in near-critical density. The fact that the energy of the laser is absorbed by majority of the electrons can be used to estimate the electron temperature T_e by balancing the plasma electron energy density and the absorbed laser energy density [22],

$$T_e[MeV] = 2.6\eta a_0^2 \frac{n_c}{n_e} \frac{\tau_0[ps]}{L[10\mu m]} \tag{2.1}$$

where τ_0 is the laser pulse duration in picoseconds, L is the target thickness, n_e is the electron density. η is the absorption coefficient which have an optimum value of 0.5 for peak electron density $n_e = a_0 n_c$ [19]. For the generation of high energetic ions, the electrons need to be heated up to MeV-ranged temperatures. The ponderomotively accelerated electrons reaching the target rear surface interacts with the unperturbed electrons at the rear end of the target and gets reflected back due to the electric field at the rear surface. The complete target heating is achieved if these hot-electrons recirculates within the target length a couple of times.

Thus, the shock formation time should be larger than the re-circulation time to achieve high shock velocity [14], ie,

$$\frac{L_{target}}{\lambda} \leq 2\pi(2-10)\frac{v_{hb}}{\lambda\omega_{pi}} = (2-10)\frac{v_{hb}}{c}\sqrt{\frac{m_i}{m_e}}\sqrt{\frac{n_c}{n_i}} \tag{2.2}$$

Higher shock velocities are obtained for targets thinner than L_{target}, where the shock front travels through the expanding target to reach its rear surface heating the target in its course. This heating time is larger for thicker targets. Thus, the target thickness and density play a decisive role in producing collisionless shock acceleration of ions. The shock acceleration mechanism is rather complicated and comparatively less explored in the near-critical regime.

2.3 PIC simulation model

For the simulations, we have used Picpsi 3D [23], a relativistic 3 dimensional PIC code developed in BARC, Mumbai. A simulation box of dimensions, $20\mu m \times 20\mu m \times 20\mu m$ consisting of $200 \times 200 \times 200$ cells is considered. A laser pulse with intensity of $1.36 \times 10^{20} W cm^{-2}$ having Gaussian profile both spatially and temporally with wavelength $1\mu m$ and laser period $T_0 = 3.3fs$ is allowed to propagate along the Z-axis. The laser pulse has a spot size (spatial FWHM) of $10\mu m$ and the laser pulse duration (FWHM) $\tau = 33fs$. The critical density for $1\mu m$ laser is $n_c = 1.1 \times 10^{21} cm^{-3}$ and the normalized vector potential for circularly polarized laser is $(\frac{a_0}{\sqrt{2}}) \approx 7$. With a relativistic intensity, the laser can penetrate the classically overdense target due to relativistically induced transparency. The electrons become relativistic in this intensity regime which increases their mass by the Lorentz factor, $\gamma = \sqrt{1 + \frac{a_0^2}{2}}$ [24]. The relativistic intensity helps the laser in propagating inside the plasma to a depth greater than the classical skin depth by a factor $\sqrt{\gamma}$. A cold and uniform density hydrogen plasma sphere is introduced inside the simulation box with an equal vacuum gap between the edge of the plasma and the sides of the simulation box. Thus the ions considered in this

study are exclusively protons with mass $m_p = 1836m_e$. Absorbing boundary conditions are used along all the three dimensions for the particles and fields. The simulations are performed with 50 particles per cell and one time-step is equal to $0.2\omega_p^{-1}$. The times are calculated after the initiation of the laser pulse inside the simulation box. A schematic of the simulation model is shown in Fig. 2.1.

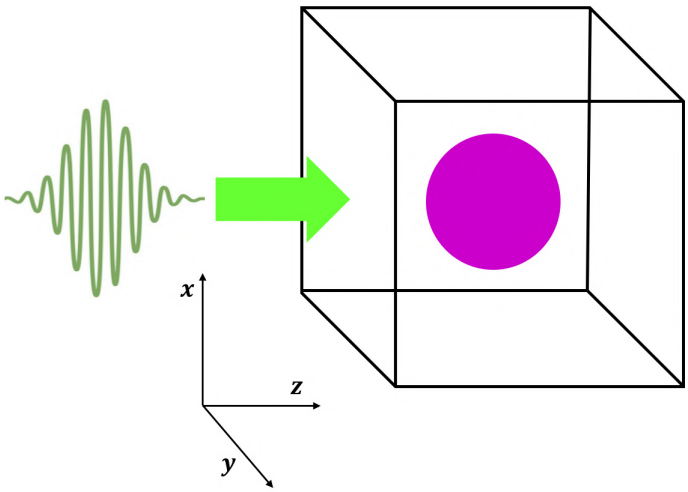

Figure 2.1: A schematic of the simulation model with the laser entering from the left side and propagating along the Z-direction.

2.4 Results and discussions

The simulations are performed keeping the plasma densities around the threshold density for relativistic transparency. At first, a circularly polarized laser is incident on a spherical plasma target of diameter $5\mu m$ with density $5n_c$. The longitudinal electric field, proton densities and the longitudinal proton momenta are plotted in Figure 2.2 at two different times: 303.55 fs and 357 fs respectively. The longitudinal electric field E_z and the longitudinal momentum p_z is normalized by E_0 and m_pc, respectively. Here, E_0 is the laser peak electric field, m_p is the mass of the proton and c is the velocity of laser in vacuum. The colour bar in the phase plots denotes the number of protons in arbitrary units (a.u.). This normalization scheme is carried out in all the subsequent

cases. A peak in the electric field in Fig 2.2(a1) is observed at the core of the target corresponding to a patch of dense beam of protons seen in Fig. 2.2(b1). This field later becomes weak at time 357 fs showing a decrease in the density of the proton region [Figs. 2.2(a2) and 2.2(b2)]. Due to the target being relativistically underdense, laser pulse could penetrate through the plasma, heat the electrons and push them due to ponderomotive force. The strong electric field formed near the core of the target signifies the possibility of the creation of a shock front. The proton phase plots of Fig 2.2(c2-c3) show the protons getting forward momentum from the rear-side target boundary due to the sheath accelerating field. However, a small number of protons are also found to be getting accelerated from the core of the target denoting shock reflection. The proton energy spectra plot (Fig 2.3) shows that the maximum energy gained by the particles goes up to 21.5 MeV.

The target diameter is now increased to $10\mu m$ keeping the density at $5n_c$. The peak of interaction occurs at around 120 fs when the target diameter is $10\mu m$. Filamentary structures of proton density are observed in the distribution plots of Fig 2.4 (a). The protons gain maximum momenta from the core of the target and are found to be accelerated by the shock front more efficiently than through the sheath mechanism. In this case, the electrons need a longer time to reach the rear side of the target, compared to the smaller target. As a result, the formation of sheath electric field at the rear side of the target is restrained to a great extent. The large population of electrons and protons accumulated at the core of the target thus forms a shock front, which reflects the protons efficiently. This is clearly visible from the proton phase plots of Fig 2.4(b) at time 357 fs. Fig 2.5 shows the time evolution of the longitudinal electric field, which indicates a shock front moving with velocity ∼0.07c. The shock velocity calculated from the graph is supported by that from theory [25] $v_s \sim v_p = \frac{a_0}{\sqrt{2}} c \sqrt{\frac{Z m_e n_c}{A m_p n_i}} = 0.07c$. As the shock moves through the upstream plasma, it reflects the protons, which have kinetic energy lower than the electrostatic potential energy of the shock. From Equation (2.1) the electron temperature is calculated to be 0.42

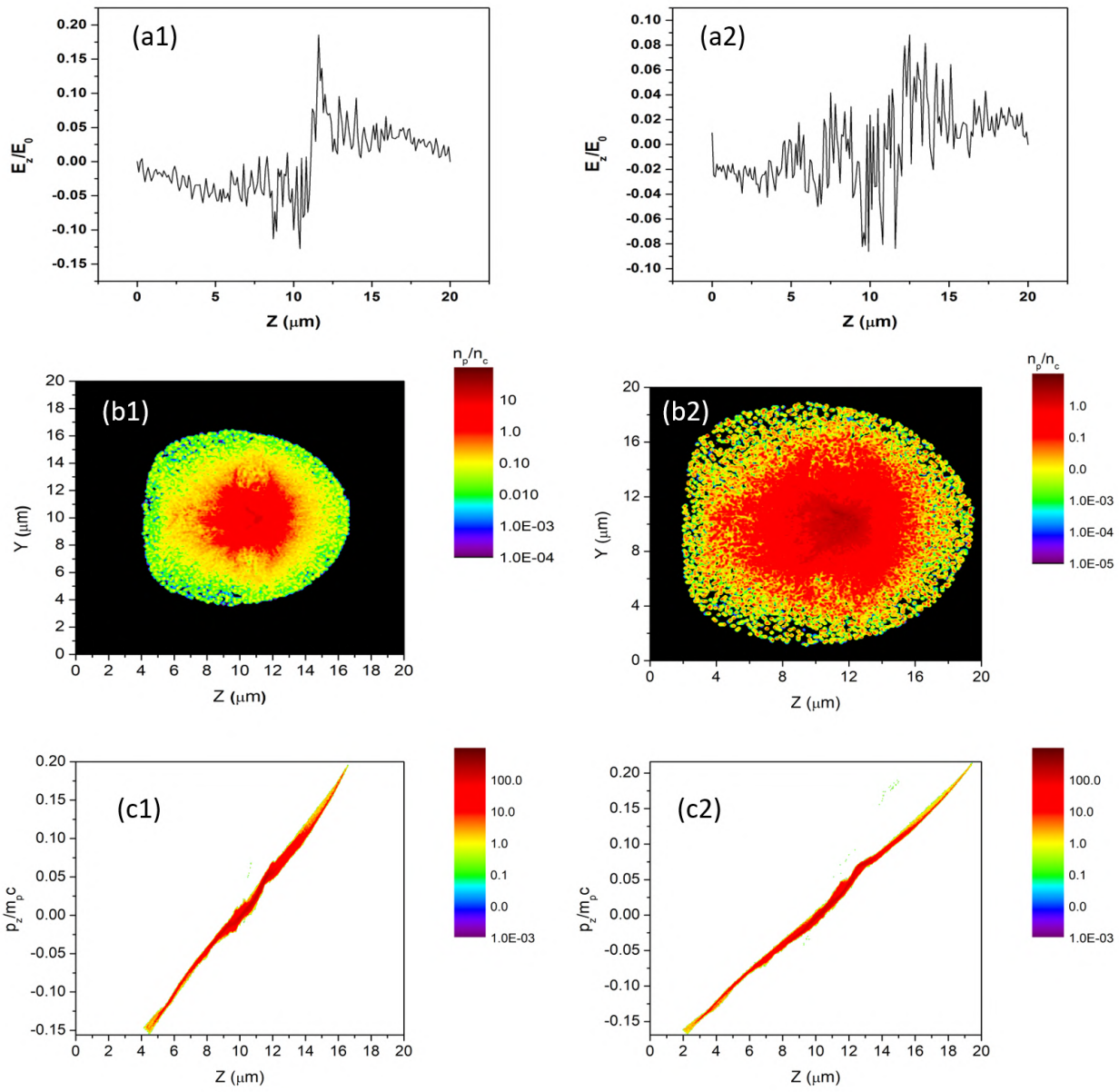

Figure 2.2: For the target with $5\mu m$ diameter and density $5n_c$: The longitudinal electric field E_z (a1-a2) along the central laser axis ; the density distribution in the central YZ plane (b1-b2); and the axial proton momentum p_z (c1-c2) along Z are at times 303.55 fs and 357 fs respectively. The colour bar at (c1-c2) denotes the number of protons in arbitrary units (a.u.).

MeV. The ion acoustic velocity is found to be $c_s = \sqrt{\frac{ZT_e}{Am_p}} = 0.02c$. Using the shock velocity, the Mach number of the shock front is found to be $M \sim 3.5$.

In order to see the effect of target density, the simulation is repeated

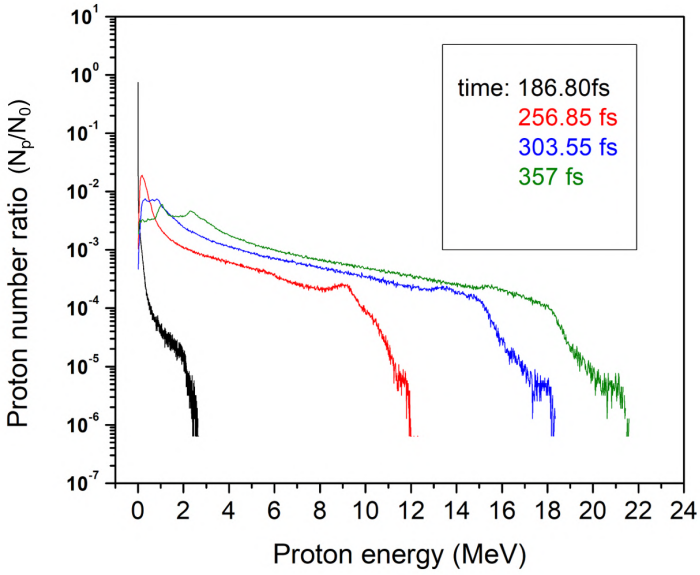

Figure 2.3: The proton energy spectrum at different times for the target with density $5n_c$ and diameter $5\mu m$. The proton number is normalized by the total number of protons.

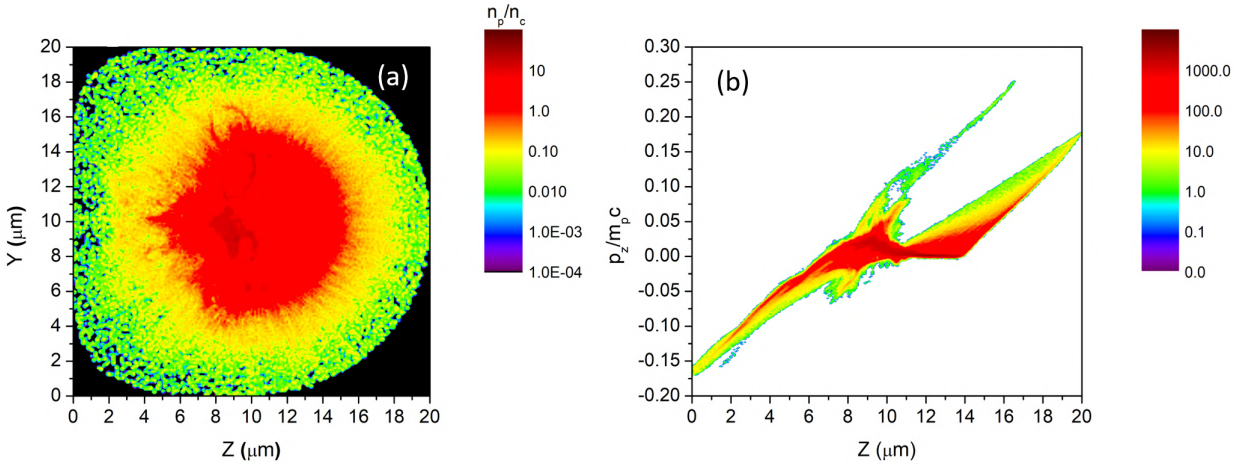

Figure 2.4: For the target with $10\mu m$ diameter and density $5n_c$: The proton density distribution in the central YZ plane (a); and the axial momentum p_z (b) along Z are plotted at 357 fs.

for $5\mu m$ target with $7n_c$ density. The proton distribution plot shows a collimated beam at time 276.5 fs [Fig. 2.6(a1)] which is emitted from the rear side of the plasma at a later time 355.5 fs [Fig. 2.6(a2)]. The protons gain momentum in Fig. 2.6(b1) from the target centre at 276.5 fs due to the formation of shocks. The phase space plots clearly show

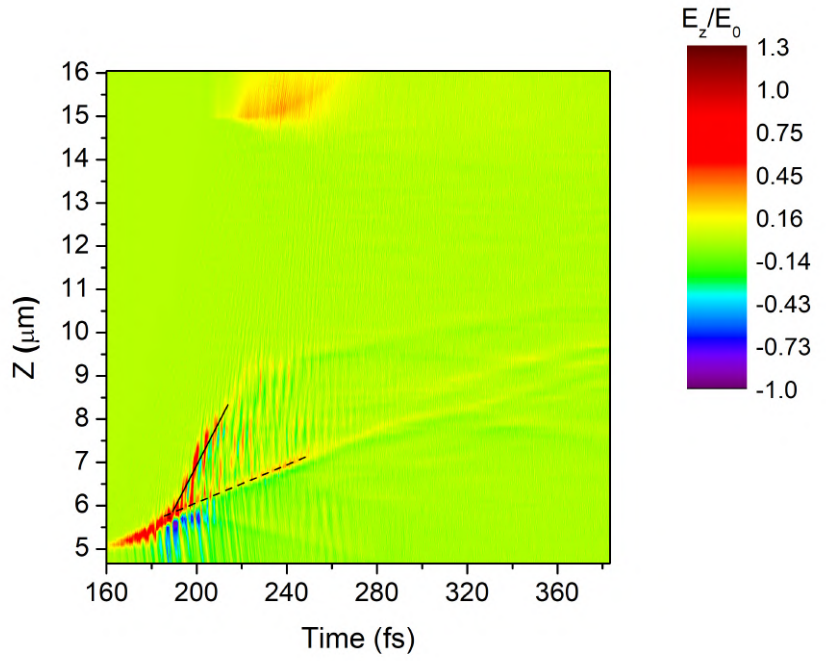

Figure 2.5: The normalized axial electric field variation along the laser propagation direction Z and time for the target with density $5n_c$ and diameter $10\mu m$. The dotted line denotes the shock front while the solid line denotes the reflected protons.

that the protons are accelerated both by TNSA as well as shock potential at time 355.5 fs [Fig. 2.6(b2)]. The shock accelerated protons are found to be more dominant than those accelerated by TNSA mechanism. The proton energy spectrum, shown in Fig 2.7(a) reveals that the maximum energy achieved in this case is around 40 MeV, with clear plateau structures visible, which are a signature of shock acceleration. From Fig 2.7(b), the velocity of the shock front is found to be $v_s \sim 0.056c$ which is supported by the shock velocity calculated from theory, $v_s \sim 0.06c$. The ion acoustic velocity is found to be 0.025c with the shock front moving with Mach number $M \sim 2.4$. This is in accordance with the M value predicted in the paper by Pak *et al* [19]. The velocity of the protons reflected from the shock front is $v_{protons} \sim 0.18c$ from Fig 2.7(b) (solid line), which is greater than twice the shock velocity. The additional acceleration is due to the sheath field, i.e. $v_f = 2v_s + v_{sheath}$ as in Section 2.2.

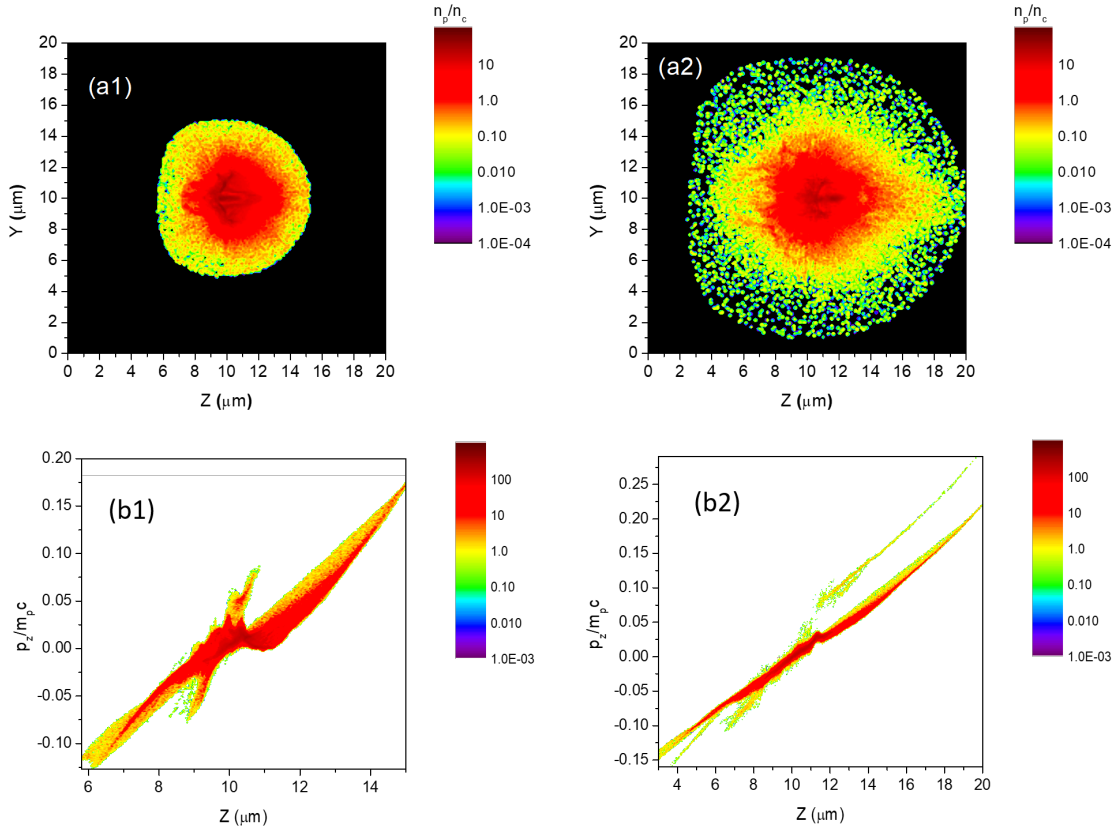

Figure 2.6: The proton density distribution in the central YZ plane (a1-a2); and the axial momentum p_z along Z (b1-b2) at times 276.5 fs and 355.5 fs for the target with $5\mu m$ diameter and density $7n_c$.

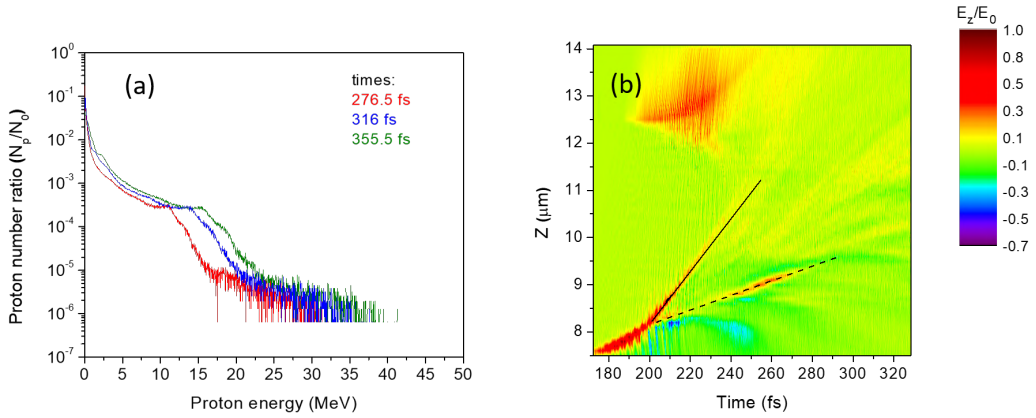

Figure 2.7: (a) The spatio-temporal evolution of the longitudinal electric field (E_z) along the central laser axis. (b) is the proton energy spectra at different times. The plasma target conditions are similar to Figure 2.5.

The results for the $5\mu m$ spherical targets with $7n_c$ density is compared with that of a rectangular target having the same dimension and density.

The distinct collimated proton beam observed for the sphere target is not observed in this case (Fig. 2.8(a)). The energy spectra plot [Fig. 2.8(b)] shows a continuous variation of proton numbers with energy without any sign of a mono-energetic beam. The maximum achievable energy is found to be $\sim 32MeV$ which is less than the case of the spherical target. The spherical geometry of the target thus facilitates the formation of shock structures. The curved surface of the spherical target contributes to the formation of a collimated mono-energetic proton beam, whereas the curved rear surface suppresses the formation of the sheath field at the rear surface. As a result, TNSA is found to be less effective than shock acceleration in the spherical case. At a later time filamentation of the proton beam takes place and thus the collimated proton beam gradually dissipates. However, with a proper choice of plasma parameters, it may be possible to observe shock acceleration in rectangular targets.

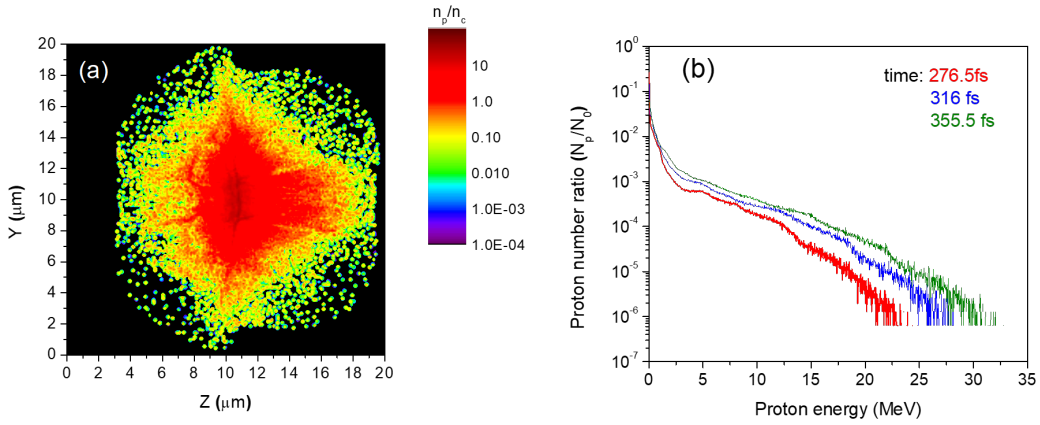

Figure 2.8: (a) The proton density distribution in the central YZ plane at time 355.5 fs; and (b) the proton energy spectra at different times for the flat (rectangular) target with dimensions $5\mu m$ and density $7n_c$:

For a relativistically overdense target with density $10n_c$ and target diameter equal to the laser FWHM ($10\mu m$), the peak of the laser hits the target at around 113 fs. This time is referred to as the laser peak interaction time [6]. A dense region is observed at the front side of the target which further increases and propagates forward at time 280.84 fs in Fig 2.9(a). The corresponding phase space plot [Fig. 2.9(b)] in-

dicates that protons gain maximum momentum due to the RPA mechanism. The ion energy spectra plotted in Fig 2.9(c) show the appearance of a plateau at time 247.8 fs, which may indicate the presence of an acceleration mechanism other than TNSA. At later time , however, this peak vanishes. The peak electric field appearing in the rear side further accelerates the protons through TNSA mechanism. The simulation for the same target is also performed with a linearly polarized laser. The purple curve in Fig 2.9(c) shows that the maximum energy achieved with the linearly polarized laser is about 7 MeV, whereas, for circularly polarized laser it is found to be about 16 MeV.

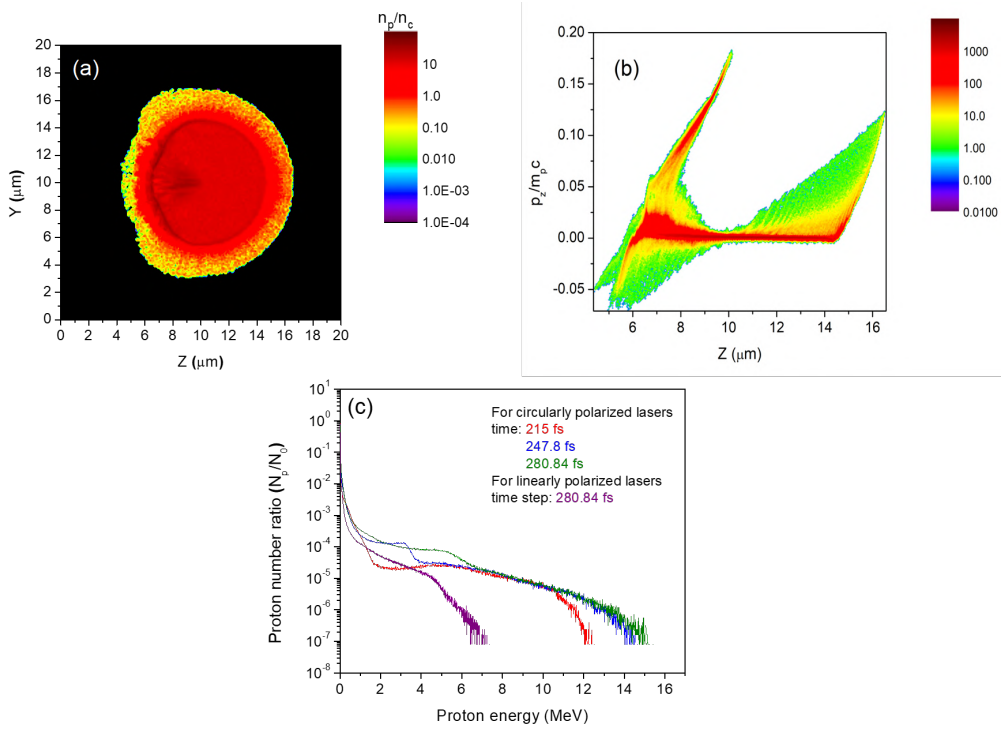

Figure 2.9: (a) The proton density distribution in the central YZ plane and (b) the axial momentum p_z along Z are plotted at 280.84 fs. (c) is the proton energy spectra at different times. The purple line denotes the energy spectrum at 280.84 fs using a linearly polarized laser. The target is of diameter $10\mu m$ and density $10n_c$.

Fig 2.10(a) represents electron density distribution in the central YZ plane at time 215 fs. Two electron bunches are emitted from the plasma sphere with diameter $10\mu m$ and density $10n_c$. Here the laser FWHM is of the order of the dimension of the plasma sphere. Usually when a

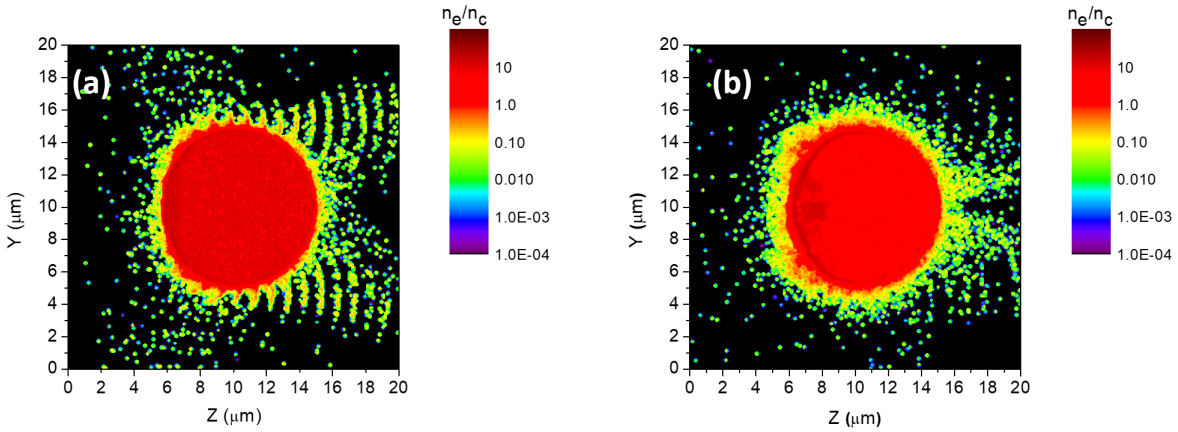

Figure 2.10: The electron density distribution in the central YZ plane at 215 fs for the targets with diameter $10\mu m$ and density (a) $10n_c$ nad (b) $7n_c$.

p-polarized electromagnetic wave is incident obliquely on a steep plasma boundary, the electrons are dragged into the vacuum and sent back to the plasma. Although in the present work, circularly polarized laser is used, the formation of electron bunches may still be attributed to the Brunel mechanism [26]. Both Fig 2.10(a) and Fig. 2.11(b) reveal that hot electron bunches are emitted from the plasma target with spatial period $\sim 1\mu m$ which is the laser wavelength. In the phase space density plot of Fig 2.11 (b), the Z-components of momenta of only the top bunch of electrons is plotted. The emission of hot electrons from a plasma target may be due to interplay between vacuum heating as well as $\overrightarrow{v} \times \overrightarrow{B}$ mechanism. Although for circularly polarized laser, $\overrightarrow{v} \times \overrightarrow{B}$ term vanishes, there may be still emission of hot electrons from the plasma sphere due to the interaction of electrons with the self generated magnetic field [27, 28]. However, the periodic hot electron bunches emitted in this case is caused mainly by vacuum heating. When the laser pulse is focused to a small spot with size comparable to the laser wavelength, the longitudinal component of the laser field cannot be neglected. The longitudinal field may significantly affect the electron motion and cause ejection of electrons from the periphery of the target via vacuum heating [29]. The appearance of these two electron bunches is suppressed in the lower density target ($7n_c$) [Fig 2.10(b)]. For the target with density $7n_c$, the laser may penetrate the target due to relativistic transparency

and the effect of vacuum heating gets suppressed. The presence of these electron bunches have a negative impact on the maximum proton energy achieved. The hot electrons bunches emitted from the edges of the target heats up the target in the transverse direction inhibiting the forward acceleration of protons in an effective manner. From the phase space plots of Fig 2.11(a) it is clearly visible that the electrons attain relativistic velocities as soon as the laser effectively interacts with the plasma.

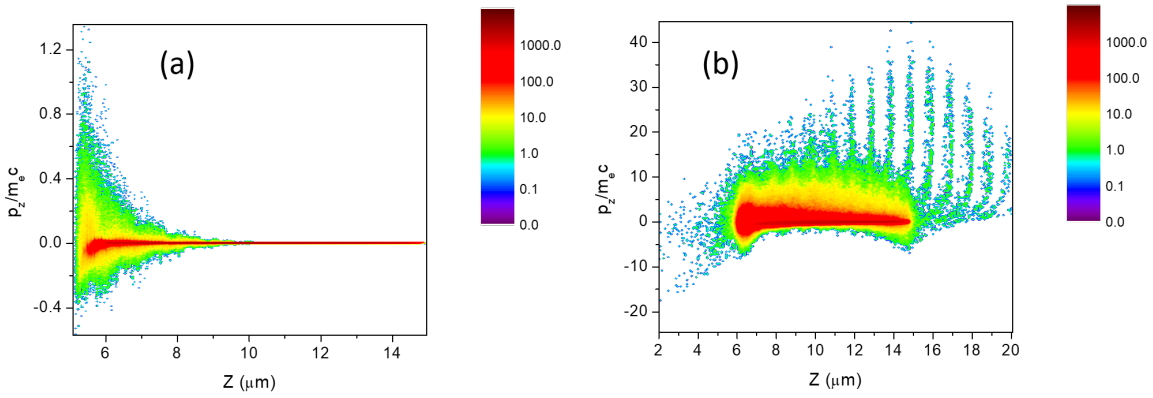

Figure 2.11: The longitudinal electron phase space plots along the propagation axis Z for the target with diameter $10\mu m$ and density $10n_c$ at times (a) 155.3 fs and (b) 215 fs. In (b) the Z-components of momenta of only the top bunch of electrons is plotted.

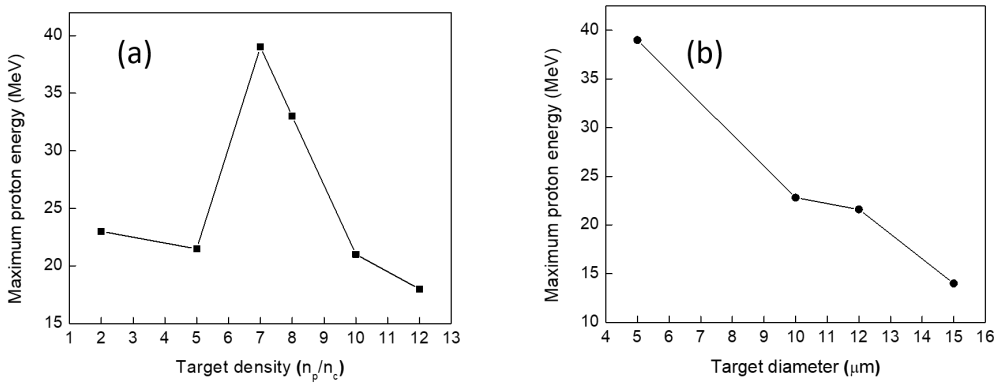

Figure 2.12: For the target with $10\mu m$ diameter and density $5n_c$: The proton density distribution in the central YZ plane (a); and the axial momentum p_z (b) along Z are plotted at 357 fs.

Based on the simulation results, the variation of maximum proton energy with the density is plotted for the target sphere with diameter $5\mu m$ in

Fig 2.12(a). It is observed that proton energy is maximum for the target with density $7n_c$. The combined effect of all the three acceleration processes pushes the protons forward to obtain such high values of energies. For this optimum density value, the variation of the proton energy with the target diameter is plotted in Fig 2.12(b). The smallest target diameter ($5\mu m$) facilitates the production of protons having highest energies. As the target diameter increases, the electron heating becomes substantially less and the target cools down rapidly. Thus electron recirculations could not take place efficiently in such cases leading to a decrease in the energy of the proton beam.

2.5 Conclusion

In this chapter, the possibility of ion acceleration in a spherical plasma target in near-critical regime has been explored, using circularly polarized laser beam. For understanding the role of target geometry and laser polarization, a comparative study has been made with the results of rectangular target of similar dimension. Several novel features of ion acceleration have been observed from the present study. Ions are found to be accelerated due to the interplay among RPA, shock and TNSA mechanisms. Different target parameters (density, size, and shape) and laser polarizations are used to attain an optimum set of parameters where a maximum value of peak energy is obtained. It is observed that these parameters work in synergy to generate the highly energetic jet of protons.

The results of this chapter can be summarized in the following points:

1. The target geometry is found to play a major role on the maximum energy attained by the protons. This energy further depends on target size and density. The quality of the proton beam both in terms of energy and mono-energetic nature is superior than the proton beam obtained from the corresponding rectangular target of same size. A combination of RPA, shock acceleration and TNSA contributes to such high values of energy. The proton beam colli-

mation is also better in the spherical case. The curved front surface of the sphere target focuses the accelerated protons into a beam of lower divergence. This effect is not seen in the case of the flat target.

2. Proton acceleration through shock mechanism is found to be dominant for targets with relativistically critical densities. In such cases, the Mach number is found to be well within in the range for electrostatic shocks $1.5 < M < 3.5$ as given in [30]. The target with density $7n_c$ and size $5\mu m$ exhibits the optimum peak proton energy value $\sim 40MeV$. In this case the protons getting reflected by the shock front is further accelerated by the sheath field.

3. The effect of RPA increases with the increase in target size and density. High-density targets offer the opacity required for RPA to be dominant so that the electron heating is minimum. Moreover, the larger target size cools down the electrons so that recirculation is reduced significantly, thus promoting the effect of RPA.

4. The formation of the electron jets in larger targets at densities $7n_c$ and $10n_c$ suppresses the ion energies. The electrons gain energy from the laser beam at the target boundaries by a combination of vacuum heating and $\overrightarrow{v} \times \overrightarrow{B}$ mechanism and the plasma gets heated up in the transverse directions leading to a reduction in the proton energies. However, in this case, vacuum heating is the dominant mechanism responsible for the emission of periodic electron bunches.

We have observed that the protons accelerated due to shocks at the core may be further accelerated due to the sheath formation in the rear surface. An effort has been made to identify the shock dominant regimes. Near-critically dense spherical plasma target may be a promising way to obtain compact proton accelerators.

Bibliography

[1] Limpouch, J., Psikal, J., Andreev, A., Platonov, K. Y., and Kawata, S. Enhanced laser ion acceleration from mass-limited targets. *Laser Part. Beams.*, 26(2):225–234, 2008.

[2] Sokollik, T., Paasch-Colberg, T., Gorling, K., Eichmann, U., Schnürer, M., Steinke, S., Nickles, P., Andreev, A., and Sandner, W. Laser-driven ion acceleration using isolated mass-limited spheres. *New J. Phys.*, 12(11):113013, 2010.

[3] Zheng, J., Sheng, Z. M., Peng, X. Y., and Zhang, J. Energetic electrons and protons generated from the interaction of ultrashort laser pulses with microdroplet plasmas. *Phys. Plasmas*, 12(11):113105, 2005.

[4] Yu, W., Xu, H., He, F., Yu, M., Ishiguro, S., Zhang, J., and Wong, A. Direct acceleration of solid-density plasma bunch by ultraintense laser. *Phys. Rev. E*, 72(4):046401, 2005.

[5] Kemp, A. and Ruhl, H. Multispecies ion acceleration off laser-irradiated water droplets. *Phys. Plasmas*, 12(3):033105, 2005.

[6] d'Humières, E., Lefebvre, E., Gremillet, L., and Malka, V. Proton acceleration mechanisms in high-intensity laser interaction with thin foils. *Phys. Plasmas*, 12(6):062704, 2005.

[7] Kuri, D. K., Das, N., and Patel, K. Role of target thickness in proton acceleration from near-critical mass-limited plasmas. *Appl. Phys. B*, 123(7):201, 2017.

[8] Li, Y., Zhang, J., Sheng, Z., Teng, H., Liang, T., Peng, X., Lu, X., Li, Y., and Tang, X. Spatial distribution of high-energy electron emission from water plasmas produced by femtosecond laser pulses. *Phys. Rev. Lett.*, 90(16):165002, 2003.

[9] Liseykina, T., Pirner, S., and Bauer, D. Relativistic attosecond electron bunches from laser-illuminated droplets. *Phys. Rev. Lett.*, 104(9):095002, 2010.

[10] Henig, A., Kiefer, D., Geissler, M., Rykovanov, S. G., Ramis, R., Hörlein, R., Osterhoff, J., Major, Z., Veisz, L., Karsch, S., et al. Laser-driven shock acceleration of ion beams from spherical mass-limited targets. *Phys. Rev. Lett.*, 102(9):095002, 2009.

[11] Kluge, T., Enghardt, W., Kraft, S., Schramm, U., Zeil, K., Cowan, T., and Bussmann, M. Enhanced laser ion acceleration from mass-limited foils. *Phys. Plasmas*, 17(12):123103, 2010.

[12] Ostermayr, T. M., Haffa, D., Hilz, P., Pauw, V., Allinger, K., Bamberg, K.-U., Böhl, P., Bömer, C., Bolton, P., Deutschmann, F., et al. Proton acceleration by irradiation of isolated spheres with an intense laser pulse. *Phys. Rev. E*, 94(3):033208, 2016.

[13] Liu, M., Weng, S., Li, Y., Yuan, D., Chen, M., Mulser, P., Sheng, Z., Murakami, M., Yu, L., Zheng, X., et al. Collisionless electrostatic shock formation and ion acceleration in intense laser interactions with near critical density plasmas. *Phys. Plasmas*, 23(11):113103, 2016.

[14] Silva, L. O., Marti, M., Davies, J. R., Fonseca, R. A., Ren, C., Tsung, F. S., and Mori, W. B. Proton shock acceleration in laser-plasma interactions. *Phys. Rev. Lett.*, 92(1):015002, 2004.

[15] Macchi, A., Cattani, F., Liseykina, T. V., and Cornolti, F. Laser acceleration of ion bunches at the front surface of overdense plasmas. *Phys. Rev. Lett.*, 94(16):165003, 2005.

[16] He, M. Q., Dong, Q. L., Sheng, Z. M., Weng, S. M., Chen, M., Wu, H. C., and Zhang, J. Acceleration dynamics of ions in shocks and solitary waves driven by intense laser pulses. *Phys. Rev. E*, 76(3):035402, 2007.

[17] Fiuza, F., Stockem, A., Boella, E., Fonseca, R., Silva, L., Haberberger, D., Tochitsky, S., Mori, W., and Joshi, C. Ion acceleration

from laser-driven electrostatic shocks. *Phys. Plasmas*, 20(5):056304, 2013.

[18] Stockem, A., Boella, E., Fiuza, F., and Silva, L. Relativistic generalization of formation and ion-reflection conditions in electrostatic shocks. *Phys. Rev. E*, 87(4):043116, 2013.

[19] Pak, A., Kerr, S., Lemos, N., Link, A., Patel, P., Albert, F., Divol, L., Pollock, B., Haberberger, D., Froula, D., et al. Collisionless shock acceleration of narrow energy spread ion beams from mixed species plasmas using 1 μ m lasers. *Phys. Rev. ST Accel. Beams*, 21(10):103401, 2018.

[20] Liu, M., Xie, B., Huang, Y., Liu, J., and Yu, M. Enhanced ion acceleration by collisionless electrostatic shock in thin foils irradiated by ultraintense laser pulse. *Laser Part. Beams.*, 27(2):327–333, 2009.

[21] Kim, Y. K., Cho, M. H., Song, H. S., Kang, T., Park, H. J., Jung, M. Y., and Hur, M. S. Shock ion acceleration by an ultrashort circularly polarized laser pulse via relativistic transparency in an exploded target. *Phys. Rev. E*, 92(4):043102, 2015.

[22] Fiuza, F., Stockem, A., Boella, E., Fonseca, R., Silva, L., Haberberger, D., Tochitsky, S., Gong, C., Mori, W., and Joshi, C. Laser-driven shock acceleration of monoenergetic ion beams. *Phys. Rev. Lett.*, 109(21):215001, 2012.

[23] Upadhyay, A., Patel, K., Rao, B., Naik, P., and Gupta, P. Three-dimensional simulation of laser–plasma-based electron acceleration. *Pramana*, 78(4):613–623, 2012.

[24] Macchi, A. *A Superintense Laser-Plasma Interaction Theory Primer*. Springer Science & Business Media, 2013.

[25] Schlegel, T., Naumova, N., Tikhonchuk, V., Labaune, C., Sokolov, I., and Mourou, G. Relativistic laser piston model: Ponderomotive ion acceleration in dense plasmas using ultraintense laser pulses. *Phys. Plasmas*, 16(8):083103, 2009.

[26] Brunel, F. Not-so-resonant, resonant absorption. *Phys. Rev. Lett.*, 59(1):52, 1987.

[27] Najmudin, Z., Tatarakis, M., Pukhov, A., Clark, E., Clarke, R., Dangor, A., Faure, J., Malka, V., Neely, D., Santala, M., et al. Measurements of the inverse faraday effect from relativistic laser interactions with an underdense plasma. *Phys. Rev. Lett.*, 87(21):215004, 2001.

[28] Qiao, B., He, X., and Zhu, S.-p. Fluid theory for quasistatic magnetic field generation in intense laser plasma interaction. *Phys. Plasmas*, 13(5):053106, 2006.

[29] Berezhiani, V. and Shatashvili, N. On the "vacuum heating" of plasma in the field of circularly polarized laser beam. *Eur. Phys. Lett*, 76(1):70, 2006.

[30] Forslund, D. and Shonk, C. Formation and structure of electrostatic collisionless shocks. *Phys. Rev. Lett.*, 25(25):1699, 1970.